Materials & Design 225 (2023) 111462

Contents lists available at ScienceDirect

Materials & Design

journal homepage: www.elsevier.com/locate/matdes

Influence of the deposition process on the Cr_2AlC phase formation during heat treatment of Cr-Al-C thin films

Stefan Heinze [a,*], Andreas Stark [b], Julius Hendl [a,c], Christoph Leyens [a,c]

[a] Technische Universität Dresden, Institute of Materials Science IfWW, Helmholtzstr. 7, 01069 Dresden, Germany
[b] Helmholtz-Zentrum Hereon, Institute of Materials Physics, Max-Planck-Str. 1, 21502 Geesthacht, Germany
[c] Fraunhofer Institute for Material and Beam Technology IWS, Winterbergstr. 28, 01277 Dresden, Germany

GRAPHICAL ABSTRACT

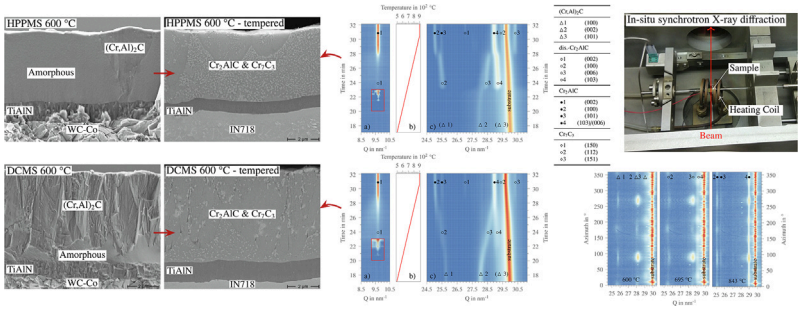

ARTICLE INFO

Article history:
Received 3 July 2022
Revised 1 December 2022
Accepted 2 December 2022
Available online 8 December 2022

Keywords:
Cr_2AlC phase formation
Metastable $(Cr,Al)_2C$
Metastable disordered-Cr_2AlC
Amorphous Cr-Al-C
In-situ X-ray diffraction
Thin films

ABSTRACT

This paper focuses on the Cr_2AlC phase formation during annealing post-treatment, with amorphous Cr-Al-C and $(Cr,Al)_2C$ as initial phases in the as-deposited state. The influence of the deposition process on the Cr_2AlC formation, texture, and phase composition is investigated and an in-depth discussion of the intermediate phase is carried out. Cr-Al-C thin films were deposited by Direct Current Magnetron Sputtering and High Power Pulsed Magnetron Sputtering with the variation of the deposition temperature. To investigate the microstructure, phase composition, and texture, in situ synchrotron and high-temperature X-ray diffraction experiments were conducted and accompanied by electron microscopy. The Cr_2AlC formation can be described as a temperature and time-dependent process with one intermediate state characterized by the formation of the disordered-Cr_2AlC phase. Disordered-Cr_2AlC shows a similar unit cell to Cr_2AlC with an increased c/a ratio. The ratio decreases during the phase formation resulting from an ordering process. Formation temperatures depend on the initial phase, with a decreased formation temperature for $(Cr,Al)_2C$, and the deposition process. While the (002) fiber texture of $(Cr,Al)_2C$ inherited to Cr_2AlC, Cr_2AlC originated from amorphous Cr-Al-C showed no preferred orientation. The coatings contained Cr_7C_3 as an additional phase, dependent on the deposition process and initial phases.

1. Introduction

Cr_2AlC, a representative of the MAX phases, is characterized by a unique combination of metal and ceramic properties. In particular, the oxidation resistance – as a result of the selective Al oxidation – is to be emphasized in comparison to other MAX phases.

* Corresponding author.
E-mail addresses: stefan.heinze@tu-dresden.de (S. Heinze), andreas.stark@hereon.de (A. Stark), julius.hendl@tu-dresden.de (J. Hendl), christoph.leyens@iws.fraunhofer.de, christoph.leyens@tu-dresden.de (C. Leyens).

https://doi.org/10.1016/j.matdes.2022.111462
0264-1275/

Cr_2AlC thin films are often synthesized by physical vapor deposition (PVD) techniques like Direct Current Magnetron Sputtering (DCMS) and High Power Pulsed Magnetron Sputtering (HPPMS) [1–4]. The deposition process parameters enable the variation of the kinetic energy of the sputtered flux and substrate temperatures, resulting in a wide range of possible coating properties. Textured coatings with broader columnar microstructure as well as very dense coatings with a fine microstructure, without columnar growth and texturing, are feasible [5]. As a result of the combination of the kinetic energy of the sputtered flux and thermal energy of the substrate, the Cr_2AlC formation temperature can be reduced significantly compared to the formation by an annealing post-treatment of metastable or amorphous Cr-Al-C coatings. The lowest reported temperatures for Cr_2AlC during deposition are 300 °C, for a Ti-Cr-Al-C coating, and 450 °C for Cr-Al-C coatings [6,7].

Metastable phases and amorphous coatings are achievable, if the kinetic energy of the sputtered flux and the thermal energy on the substrate surface, provided during the deposition process, is too low for the formation of a stable phase [3,6,8]. Shtansky et al. [6] first described a metastable $(Cr,Al)_2C$ phase, a solid solution of Al in hexagonal Cr_2C (space group $P6_3/mmc$, prototype Mo_2C [9]), present in Cr-Al-C coatings deposited at 300 °C substrate temperature. The formation of the metastable $(Cr,Al)_2C_x$ phase – with a similar space group and prototype as $(Cr,Al)_2C$ –, as the intermediate phase during an annealing post-treatment of amorphous Cr-Al-C coatings, was reported by Abdulkadhim et al. [8]. Because the $(Cr,Al)_2C$ and $(Cr,Al)_2C_x$ phases have a similar crystal structure, both metastable phases share essentially the same diffraction peaks, with slightly different diffraction peak positions due to the different determined lattice parameter – $(Cr,Al)_2C$ with a = 2.79 Å and c = 4.46 Å [6], $(Cr,Al)_2C_x$ with a = 2.825 Å and c = 4.353 Å [8]. Both phases show a decreased lattice parameter c in the range of 1/3 of Cr_2AlC (c_{Cr_2AlC}=12.82 Å), resulting in the shift of the (002) and (101) reflection to higher diffraction angles, whereby these two diffraction peaks are the distinctive feature between these metastable phases and Cr_2AlC [6,8]. During the last years, mainly $(Cr,Al)_2C_x$ was used to describe the metastable state of Cr_2AlC coatings in the as-deposited state and as an intermediate phase of the Cr_2AlC formation process. However, no distinct differences are published up to the present [6,8].

A disordered Cr_2AlC phase with a decreased a (a_{Cr_2AlC}=2.863 Å to $a_{disordered\,Cr_2AlC}$=2.772 Å) and increased c (c_{Cr_2AlC}= 12.82 Å to $c_{disordred\,Cr_2AlC}$=13.26 Å) lattice parameter – attributed to the partial disordering of metal atoms in Cr_2AlC – was described by Zamulaeva et al. [10] for Cr_2AlC formation via pulsed electrospark deposition but is not yet considered as an intermediate or metastable phase during Cr_2AlC phase formation.

The Cr_2AlC formation during a annealing post-treatment from an amorphous as-deposited state is reported to be in the temperature range of 590 °C to 600 °C, characterized by an intermediate state with a metastable phase [4,8,11].

The present work investigates Cr_2AlC formation in dependence on the deposition process from a metastable as-deposited state, with the amorphous and $(Cr,Al)_2C$ phases present. The focus is set on the in-depth description of the intermediate state, possible influences on the formation temperatures, and the phase composition after the formation. This paper is the continuation of the first article [12], investigating the influence of the deposition process and substrate on the microstructure, phase composition, and residual stress on as-deposited Cr-Al-C coatings.

2. Materials and methods

2.1. Coating deposition

Thin films of about 5 µm thickness were deposited by HPPMS and DCMS at chamber temperatures of 600 °C and 700 °C in the industrial-sized coater Kobelco S40 by KCS Europe GmbH. A summary of the main deposition parameters is given in Table 1.

Of the coatings investigated in the first paper of the series [12], these three were chosen to investigate a wide range of coating properties. It was not possible to study all coatings in the in situ experiments, so the aim was to investigate Cr-Al-C coatings with the highest amount of amorphous phase (HPPMS-600) and the lowest (DCMS-600). The HPPMS-700 coating marks a state in between the two coatings. (see Section 3.1).

The coatings were deposited on Inconel 718 (IN718) – a Ni-based superalloy [13] – and tungsten carbide-cobalt (WC–Co) of grade K40UF with 10 wt.% Co and 0.6 µm WC grain size. Further information regarding the characteristics of the deposition process, like influences on the actual deposition temperature, can be found in the first paper of the series [12].

Investigations regarding phase formation were performed at temperatures up to 900 °C. To prevent interdiffusion between the substrate and the Cr-Al-C coatings, a 1 µm TiAlN interdiffusion barrier – 29 at.% Ti, 25 at.% Al and 46 at.% N – was applied for IN718 and WC–Co substrates. The TiAlN coatings were deposited in the Kobelco S40 coater using Arc-PVD with a chamber temperature of 600 °C and −50 V bias.

2.2. Coatings characterization, in situ experiments, and annealing post-treatment

2.2.1. Electron microscopy for microstructure analysis

The cross-section preparation via grinding and polishing of the tempered samples was performed on the IN718 samples because the lower hardness compared to WC–Co led to an improved finish of the cross-section. Imaging was performed with the scanning electron microscope (SEM) Zeiss DSM 982 Gemini with a field emission gun using a combined mode of a secondary electron detector and an Everhart–Thornley detector.

2.2.2. In-situ synchrotron and high-temperature X-ray diffraction analysis

In order to investigate the Cr_2AlC phase formation, in situ synchrotron cross-section experiments were performed at the high energy materials science beamline P07 operated by the Helmholtz-Zentrum Hereon at the light source PETRA III at DESY, Hamburg [14] – henceforth referred to as P07 experiments. The beam direction was parallel to the coating surface. The X-ray high energy of 87 keV, enabled a very high time and temperature resolution during heating and cooling, with a detector resolution of 0.007 °/pixel and ΔQ = 0.05 nm^{-1}. The 10 mm × 5 mm × 1 mm (length x width x height) samples were heat-treated in a temperature range of RT - 900 °C with a heating and cooling ramp of 30 K/min, utilizing a DIL805 A/D dilatometer from TA instruments (formerly Bähr-Thermoanalyse GmbH) with a temperature and time accuracy of ΔT = 0.05 K and Δt = 0.0005 s. A Typ S thermocouple was attached to the bottom of the sample for temperature control. The dilatometer was first evacuated and then flooded with argon. The diffraction images were taken at about every 6 K during the experiments for the IN718 substrates. Because the IN718 substrate shows fewer diffraction peak overlapping with the coating

Table 1
Overview of deposition parameters for used coatings.

Coating	HPPMS-600	HPPMS-700	DCMS-600
Deposition process	HPPMS	HPPMS	DCMS
Chamber temperature	600 °C	700 °C	600 °C
Bias voltage	−100 V	−100 V	−70 V

phases compared to the WC–Co substrate, the IN718 results are presented in this paper.

Further information regarding the P07 experiment can be found in the first paper of the series [12]. Fig. 1a gives an overview of the experimental setup in the dilatometer.

Due to the very high temperature accuracy and Q resolution in combination with the accessible complete Debye–Scherrer rings – which is necessary for textured phases –, the P07 experiments enable the phase identification during the Cr_2AlC formation. However, the constant heating rate shifts the formation temperatures to higher values compared to the formation temperatures obtained by near-equilibrium heating. In order to determine the formation temperature without this influence, high-temperature X-ray diffraction experiments – henceforth referred to as HT-XRD experiments – in the temperature range of RT - 900 °C were performed with the Bruker D8 Discover diffractometer. Cu Kα radiation was used with a Göbel mirror and 0.6 mm slit for beam parallelization and spot size decrease, as well as a Soller slit (0.12 mm plate distance) in combination with a scintillation detector. The measurements were performed in θ-2θ Bragg–Brentano geometry using a 0.025° step size and 2 s step time. In order to increase the time resolution, two smaller Q ranges for the characteristic diffraction peaks were used – Q_1 = 7.1 nm^{-1} - 10.6 nm^{-1} and Q_2 = 24.5 nm^{-1} - 31.1 nm^{-1}. The temperature chamber TC-DOME Solid from Bruker Corporation was used with a Pt20%Rh resistant heater strip and a Typ S thermocouple for temperature control. The sample placement in this chamber is shown in Fig. 1b. The experiments were performed in a high vacuum with a heating rate of 10 K/min for two different dwell times for 10 K temperature steps in the range of 500 °C to 900 °C. From 500 °C to 720 °C, 140 min dwell time was used (equal to eight diffraction pattern each for Q_1 and Q_2) to investigate the diffusion-related formation process at a constant temperature. However, for longer dwell times at high temperatures, the risk of a heater strip failure increases, whereby the dwell time was reduced to 38 min (equal to 2 diffraction pattern each for Q_1 and Q_2) from 730 °C to 900 °C. It has to be noted, that preliminary tests did not show Cr_2AlC formation-related differences for longer dwell times of 140 min for the temperature range above 720 °C.

Analysis of the synchrotron diffraction images and preparation for further investigations – frame integration and slicing – was performed with the software FIT2D [15,16]. Analysis of the integrated synchrotron frames and HT-XRD diffraction pattern was performed with Match!3 from CRYSTAL IMPACT [17] for phase identification and Rietveld refinement. The phases Cr_2AlC [18], Cr_7C_3 [19], and $(Cr,Al)_2C$ [20] were calculated on basis of data from Springer Materials. The data for the crystallographic structure of the substrates were used from data provided by Match!3 on basis of the Crystallography Open Database (COD) [21].

Because the P07 and HT-XRD experiments were performed with different photon energies, the results in this paper are given in fundamental unit $Q = 4\pi\frac{\sin(\theta)}{\lambda}$ to obtain comparability.

2.2.3. Annealing post-treatment

In order to analyze the microstructure and phase composition after the finished Cr_2AlC phase formation, an annealing post-treatment with the as-deposited coatings at 800 °C and 1 h dwell time was carried out. The samples were heated with 10 K/min to the target temperature in a tube furnace and furnace cooling was used. During the treatment, the samples were shrouded by constant argon flow.

3. Results and discussion

3.1. As-deposited state

In this section, a short overview of the microstructure and phase composition of the Cr-Al-C coatings in the as-deposited state, with the focus on relevant information regarding the phase formation, will be given. The in-depth description can be found in the first paper of the series [12].

Fig. 2 shows the cross-section of the HPPMS-600 (Fig. 2a), HPPMS-700 (Fig. 2b), and DCMS-600 (Fig. 2c) coatings in the as-deposited state on WC–Co substrate with a TiAlN interdiffusion barrier. The average thickness of the HPPMS coatings is 4.6 µm and that of the DCMS-600 coating is 5.7 µm. In general, these coatings are characterized by cone-like crystalline and amorphous areas.

As a result of the higher kinetic energy of the sputtered flux for the HPPMS process compared to DCMS – resulting in an increased renucleation and thereby in the decrease of heterogeneous nucleation sites, where nuclei can grow further, for lower average deposition temperatures [6,22] –, the HPPMS-600 coating consists of mainly amorphous phase. For the HPPMS-700 coatings, the higher deposition temperature leads to the increase of growable heterogeneous nuclei and thus to an increased coating crystallinity. The DCMS-600 coating shows the highest crystallinity because the kinetic energy of the DCMS process is greatly decreased compared to the HPPMS process [5].

The crystalline area microstructure is dependent on the deposition process and deposition parameters. The HPPMS process and high bias voltage lead to a finer microstructure, with the possibility of the inhibition of columnar growth, compared to the DCMS process [5]. As shown in Fig. 2, the crystalline areas are characterized by a very fine-grained structure for HPPMS-600 and a broader columnar structure for DCMS-600.

The cone-like shaped crystalline areas were identified by laboratory and synchrotron X-ray diffraction analysis as the metastable

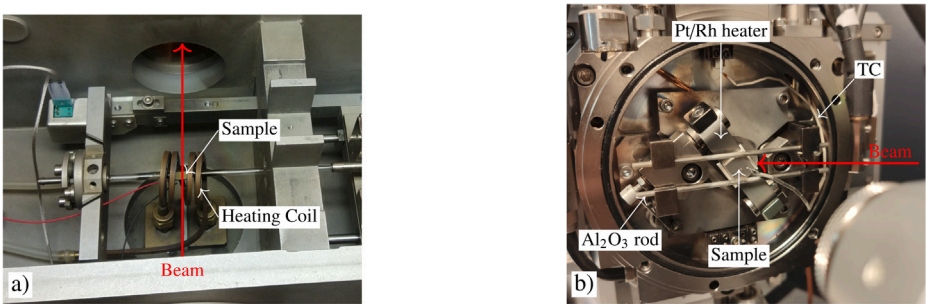

Fig. 1. (a) Overview of the sample adjustment in the dilatometer of the P07 experiment and (b) overview of the temperature chamber set-up for the HT-XRD experiments.

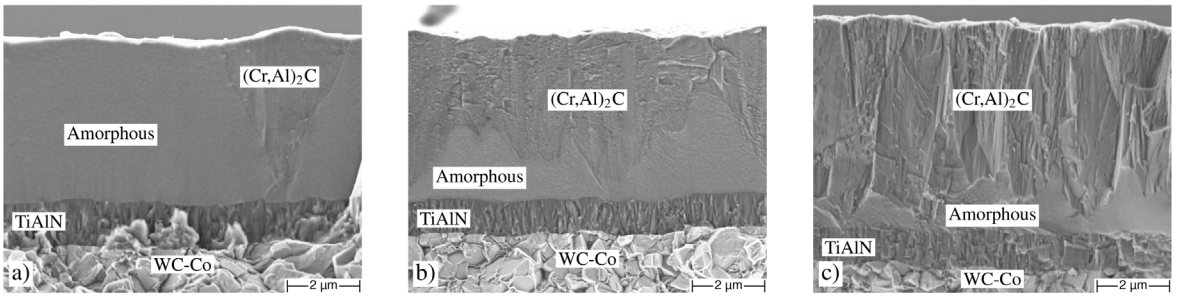

Fig. 2. SEM cross-section images of cryo-cracked (a) HPPMS-600, (b) HPPMS-700 and (c) DCMS-600 coatings with TiAlN interdiffusion barrier on WC–Co substrate in the as-deposited state. (from the first paper of the series [12]).

$(Cr,Al)_2C$ phase [6] – henceforth referred to as $(Cr,Al)_2C$. The $(Cr,Al)_2C$ solid solution originates from the hexagonal Cr_2C phase (space group $P6_3/mmc$, prototype Mo_2C [9]) where both Al and Cr atoms occupy the Cr-sites in Cr_2C [6].

The crystalline $(Cr,Al)_2C$ showed a (002) fiber texture in the as-deposited state. The influence of this texture on the Cr_2AlC phase formation is discussed in detail in Section 3.2.1 and Section 3.2.4.

It was found that the elemental composition of the three coatings as well as for the crystalline and the amorphous areas is different. The Cr and Al content with the Cr/Al ratio for the three coatings and the two distinctive crystallographic areas is summarized in Table 2. The highest mean Cr content was found for the HPPMS-700 coating, followed by the HPPMS-600 coating and the DCMS-600 coating with the lowest Cr content. It shows, that the amorphous phase has up to 3 at.% higher Cr concentration compared to the crystalline areas for the same coating. An in-depth discussion of these phenomena is given in the first paper of the series [12]. The Cr/Al ratio has a significant influence on the coatings phase composition and is discussed in Section 3.2.5.

3.2. Phase formation of Cr_2AlC

3.2.1. Cr_2AlC formation route

This section is dedicated to the Cr_2AlC phase formation of the amorphous and metastable $(Cr,Al)_2C$ phase on the examples of the HPPMS-600 and DCMS-600 coatings. Both coatings are well suited for the investigation because of the different amounts of crystalline $(Cr,Al)_2C$ and structural differences. The high amount of amorphous phase of the HPPMS-600 coating enabled the investigation of the $(Cr,Al)_2C$ to Cr_2AlC and amorphous to Cr_2AlC formation routes. The DCMS-600 coating was used to investigate the influence of the deposition parameters on the Cr_2AlC phase formation and confirm the $(Cr,Al)_2C$ to Cr_2AlC formation route.

The P07 experiments (see Section 2) provide a very high temperature and time resolution in combination with the measurement of full Debye–Scherrer rings. With this information a detailed investigation of the phase formation with consideration of texture effects and the structure of intermediate phases was possible. Because P07 experiments were performed with a constant heating rate and the phase formation is diffusion-controlled, the formation temperatures are shifted to higher values [4,8]. The HT-XRD experiments (see Section 2) represent the quasi-isothermal heat treatment to determine formation temperatures independent of the heating rate. It has to be noted, that diffusion processes may take even longer than the 140 min dwell time. However, the resistant heater strip in the temperature chamber tears for too long dwell times, thus longer dwell times were not reasonable.

Additionally, for temperatures above 800 °C, the TiAlN interdiffusion barrier failed due to high tensile residual stress as the result of the misfit of the coefficient of thermal expansion (CTE) between TiAlN and IN718 ($\alpha_{TiAlN_{RT-900°C}}$ = $8.8{\cdot}10^{-6}$ K^{-1} - $10.3{\cdot}10^{-6}$ K^{-1} [23], $\alpha_{IN718_{RT-900°C}}$ = $12.8{\cdot}10^{-6}$ K^{-1} - $17.2{\cdot}10^{-6}$ K^{-1} [13]). As a result, interdiffusion occurred between the coating and substrate, leading to depletion of Al and the transformation of Cr_2AlC to Cr-carbide [24]. For the HT-XRD, the measurements were performed in reflection geometry on the top of the coating. Considering the low average information depth of the Cu Kα radiation of approx. 2 µm - 5 µm (dependent on Q) and the initial very local interdiffusion in the vicinity of a few cracks in the TiAlN coating, the negative influence of interdiffusion on the measurement results could be prevented. Pronounced effects of the interdiffusion were found after about 4 h at 900 °C [25]. The challenges for a sufficient interdiffusion barrier and the residual stress related failure of the TiAlN interdiffusion barrier will be presented in a future paper.

Furthermore, because the HT-XRD experiments were performed in a high vacuum, longer dwell times at high temperatures led to Al depletion due to selective Al vaporization and Cr-carbide formation on the coating surface. As a result, the Cr-carbide content for temperatures in the range of 900 °C can be affected. However, this effect was not observed for the used dwell times in the relevant temperature ranges for the Cr_2AlC formation during the in situ experiments and the annealing post-treatment at 800 °C with 1 h dwell time.

Al-depletion by interdiffusion or at the coating surface was not relevant for the P07 experiments because of the high heating rate and thereby short exposure times of 4 min in the temperature range 800 °C to 900 °C, the reduced overall experiment time, and the use of an Ar atmosphere.

Fig. 3 and Fig. 4 show the results of the P07 (Fig. 3a to Fig. 3c and Fig. 4a to Fig. 4c) and the HT-XRD experiments (Fig. 3d to Fig. 3f

Table 2
Cr and Al content of the Cr-Al-C coatings obtained by cross-section EDS analysis for crystalline and amorphous areas. The values for Cr and Al in at.% consider only the Cr/Al ratio without C. (from the first paper of the series [12]).

	HPPMS-600		HPPMS-700		DCMS-600	
	crystalline	amorphous	crystalline	amorphous	crystalline	amorphous
Cr in at.%	66.9	69.9	68.9	69.5	62.3	65.5
Al in at.%	33.1	30.1	31.1	30.5	37.7	34.5
Cr/Al ratio	2.02	2.32	2.21	2.28	1.65	1.89

and Fig. 4d to Fig. 4f) for the Cr_2AlC formation HPPMS-600 and DCMS-600 in the temperature range of 500 °C to 900 °C. The two Q ranges of the heat maps represent the important characteristic reflections for the relevant phases. Additional diffraction peaks were determinable for the whole Q-range of 5–72 nm^{-1}. It has to be noted that the color scales are different for the P07 and HT-XRD heat maps. One reason is related to the different experiments. Because the HT-XRD measurements were performed in reflection geometry, only planes with a normal perpendicular to the surface as well as parallel to the incident beam to detector angle bisector contribute to the intensity of the respective diffraction peak. For the P07 cross section experiments, the whole Debye–Scherrer ring was integrated, which comprises the information of a full 360° azimuth rotation compared to the 90° direction for the HT-XRD. In particular texturing and the less intense substrate diffraction peak have a high impact on the representation of the different planes in the heat map for the P07 and HT-XRD results. Additionally, it was not possible to align the different samples for the P07 experiments equally to achieve equal substrate to coating intensity ratios. The other reason is the necessity of different color scales for the investigation of the intermediate state of the phase formation. As to be seen in the red-bordered sections in Fig. 3a and Fig. 4a, only a small intensity increase identifies the start of the formation of a different phase, which is barely recognizable in the global color scale.

3.2.1.1. Cr_2AlC phase formation - P07 experiment. Starting at 500 °C in Fig. 3a - Fig. 3c, only the $(Cr,Al)_2C$ (002) diffraction peak is visible for HPPMS-600. As the result of the low $(Cr,Al)_2C$ amount in the HPPMS-600 coating in the as-deposited state (see Section 3.1), the intensities of (100) and (101) planes are very weak and thereby not visible in the heat map, even though they are determinable in single diffraction images. In comparison, both diffraction peaks are visible for DCMS-600 at $Q \approx 25.6$ nm^{-1} and $Q \approx 29.7$ nm^{-1} in Fig. 4c.

With increasing temperature, the $(Cr,Al)_2C$ (002) diffraction peak shifts to higher Q values – against the direction of the thermal expansion, which would result in a shifting to lower Q values with increasing temperature – indicating a decrease of the lattice parameter c of $(Cr,Al)_2C$. At 632 °C an increase of this shifting in combination with a weak intensity at Q = 9.57 nm^{-1} is recognizable for HPPMS-600 (Fig. 3a to Fig. 3c). That indicates the start of the formation of an intermediate phase during the Cr_2AlC phase formation. This phase could be identified as the disordered Cr_2AlC – henceforth referred to as dis.-Cr_2AlC. An in-depth discussion of the dis.-Cr_2AlC phase and the difference to the current literature state will be given in Section 3.2.2. This first reaction is attributed to the formation of $(Cr,Al)_2C$ to dis.-Cr_2AlC.

Dis.-Cr_2AlC is structurally similar to Cr_2AlC with an increased c and decreased a lattice parameter. Even though the intensity of the

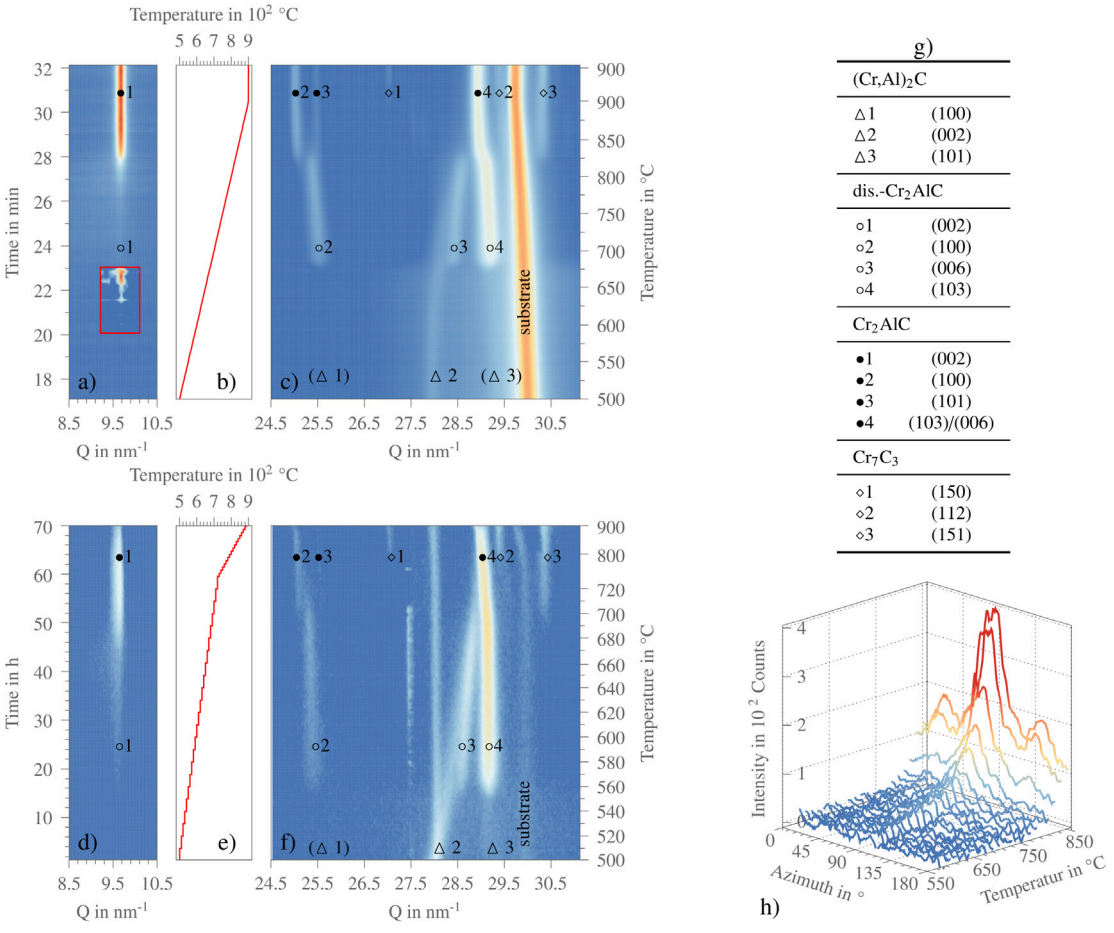

Fig. 3. Q - t heat maps showing the in situ Cr_2AlC phase formation of the HPPMS-600 coating on IN718 substrate obtained by P07 experiment (a, c) and HT-XRD using a temperature chamber (d, f). A different color scale is used for the red-bordered section in a) to reveal more details. The graphs b) and e) show the corresponding T-t curves for the respective experiment. g) summarizes the reflections marked in a), c), d) and f). h) shows the azimuth dependence of the dis.-Cr_2AlC and Cr_2AlC (002) reflection in the temperature range 585 °C - 850 °C from the P07 experiment. The color scales of the heat maps may be different in order to provide the best visualization of the results. It has to be noted, that the temperature scale in f) does not represent a linear scale and only serves as an orientation. Due to the dwell time, which is depicted in e), the range between the minor and large axis marker does not correspond to an actual temperature.

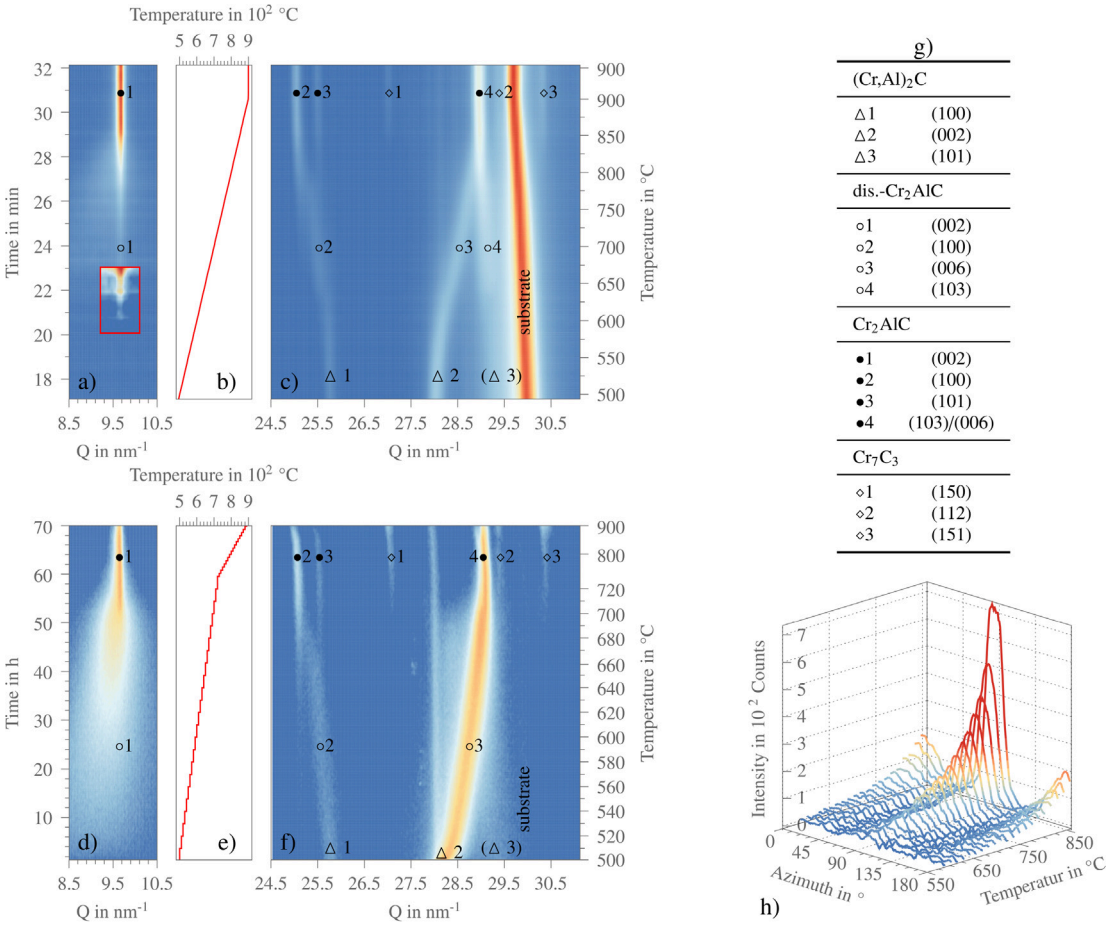

Fig. 4. *Q* - *t* heat maps showing the in situ Cr_2AlC phase formation of the DCMS-600 coating on IN718 substrate obtained by P07 experiment (a, c) and HT-XRD using a temperature chamber (d, f). A different color scale is used for the red-bordered section in a) to reveal more details. The graphs b) and e) show the corresponding T-t curves for the respective experiment. g) summarizes the reflections marked in a), c), d) and f). h) shows the azimuth dependence of the dis.-Cr_2AlC and Cr_2AlC (002) reflection in the temperature range 585 °C - 850 °C from the P07 experiment. The color scales of the heat maps may be different in order to provide the best visualization of the results. It has to be noted, that the temperature scale in f) does not represent a linear scale and only serves as an orientation. Due to the dwell time, which is depicted in e), the range between the minor and large axis marker does not correspond to an actual temperature.

dis.-Cr_2AlC (002) plane is very weak, the presence indicates a large unit cell with the *c* lattice parameter in the range of Cr_2AlC rather than $(Cr,Al)_2C$. The increased *c*/*a*-ratio results in the splitting of the (103)/(006) doublet of the Cr_2AlC phase, whereby both diffraction peaks are determinable for dis.-Cr_2AlC, see Fig. 3c. It has to be noted, that the amorphous phase transforms directly into dis.-Cr_2AlC without an additional intermediate step. This indicates, that $(Cr,Al)_2C$ is a metastable phase originating from unique conditions, present in DCMS or HPPMS deposition processes, and is not obtainable by common heat treatments.

With further temperature increase the dis.-Cr_2AlC (006) intensity (former $(Cr,Al)_2C$ (002)) shifts to higher *Q* values. At 677 °C, the three dis.-Cr_2AlC (100), (006), and (103) diffraction peaks appear in combination with a slight increase of the dis.-Cr_2AlC (002) intensity. This development is identified as the amorphous to dis.-Cr_2AlC formation. The different diffraction peak intensities for the formation of dis.-Cr_2AlC from amorphous and $(Cr,Al)_2C$ are related to the very low amount of $(Cr,Al)_2C$ in the as-deposited state. Hence, resulting in significantly lower intensities for the formation of dis.-Cr_2AlC originating from $(Cr,Al)_2C$.

The shifting of the dis.-Cr_2AlC (100), (006), and (103) diffraction peaks with further temperature increase indicates the ordering process of this phase, accompanied by increasing *a* and decreasing *c* lattice parameters (see Section 3.2.2 and a small increase of the dis.-Cr_2AlC (002) intensity. At this point of the Cr_2AlC formation, two different dis.-Cr_2AlC phases are present. This is recognizable by the different dis.-Cr_2AlC (006) positions in Fig. 3c. The diffraction peak originating from $(Cr,Al)_2C$ is located at lower *Q* values compared to the diffraction peaks of $(Cr,Al)_2C$ formed from the amorphous phase, as described in the following and Section 3.2.4. Because the diffraction peaks shifting is attributed to the ordering process, it is possible that the different *Q* values may result from a different ordering state of dis.-Cr_2AlC. However, the detailed investigation of the two phases was not part of this work. Around 770 °C, the two dis.-Cr_2AlC (006) intensities merge, and a noticeable increase of the dis.-Cr_2AlC (002) intensity can be seen in Fig. 3h. That is connected to the higher ordering state of the dis.-Cr_2AlC, see Section 3.2.2. Fig. 3h shows the dependence of the dis.-Cr_2AlC (002) intensity on the diffraction ring azimuth angle in the 585 °C to 850 °C temperature range. The intensities for the given azimuth range were averaged in the 9.64–9.69 nm^{-1} Q range with the background being subtracted.

As will be discussed in Section 3.2.4, $(Cr,Al)_2C$ shows a distinct (002) texture, which inherits to the dis.-Cr_2AlC and Cr_2AlC phases. As a result, it is possible to determine the origin of these phases by the intensity distribution of the (002) and (006) reflections over the azimuth range. The formation of dis.-Cr_2AlC/Cr_2AlC originating from $(Cr,Al)_2C$ lead to a pronounced intensity increase in the 90° azimuth direction, while the formation from the amorphous phase results in an intensity increase almost equal over the whole azi-

muth range. As to be seen in Fig. 3h, the intensity increase starts mainly in the 90° azimuth direction and may indicate the start of the dis.-Cr_2AlC to Cr_2AlC formation in the areas originating from the $(Cr,Al)_2C$ phase. This assumption is supported by the first appearance of Cr_2AlC (100) and (101) diffraction peaks at 804 °C (see Fig. 3c), while the increase of the (002) intensity for the azimuth range other than the 90° direction is noticeable at 823 °C. Further temperature increase results in the pronounced intensity increase in the 90° azimuth direction as well as the whole (002) azimuth range, indicating the ongoing ordering process and Cr_2AlC formation. More information about the Cr_2AlC and dis.-Cr_2AlC (002) intensity evolution is given in Section 3.2.2.

The Cr_2AlC formation is finished at 843 °C with the disappearance of the dis.-Cr_2AlC diffraction peaks. The relatively wide formation temperature range can be attributed to the constant heating rate of 30 K/min. As the HT-XRD experiments show (Fig. 3d to Fig. 3f), the Cr_2AlC formation is a time and temperature-dependent process, whereby constant heating will always result in a temperature range rather than a certain temperature. Additionally, weak intensities of Cr_7C_3 (150), (112), and (151) planes were determined.

The formation route for DCMS-600 is similar to HPPMS-600. However, because of the very low amount of amorphous phase in the as-deposited state, only the formation of $(Cr,Al)_2C$ to Cr_2AlC can be detected in the results, see Fig. 4. As for HPPMS-600, the start of the $(Cr,Al)_2C$ to dis.-Cr_2AlC formation is connected to the appearance of the very weak dis.-Cr_2AlC (002) intensity at 609 °C. At 628 °C several changes in Fig. 4a and Fig. 4c can be detected. Besides an increase in the dis.-Cr_2AlC (002) intensity, an increased shifting and broadening of the dis.-Cr_2AlC (100) and (006) diffraction peaks (former $(Cr,Al)_2C$ (100) and (002)), can be determined as additional characteristics for the formation of dis.-Cr_2AlC. As will be discussed in Section 3.2.2, the broadening and shifting are attributed to the disordered state. Considering the very weak dis.-Cr_2AlC (002) intensity at 609 °C in the case of DCMS-600 and the low amount of $(Cr,Al)_2C$ for HPPMS-600 – hampering the detection of this formation step –, it can be concluded, that the formation temperature for dis.-Cr_2AlC from $(Cr,Al)_2C$ is in the same range for HPPMS-600 and DCMS-600 (see Table 4 in Section 3.2.3).

During the intermediate state, the weak Cr_2AlC (100) diffraction peak appears at about 695 °C, indicating the start of the Cr_2AlC formation in some areas of the coating. This is supported by the azimuth dependence of the dis.-Cr_2AlC/Cr_2AlC (002) reflection in Fig. 4h. A steady increase of the (002) intensity is visible at about 700 °C. However, it is not possible to detect the characteristic Cr_2AlC (101) diffraction peak in this formation state because the Cr_2AlC (101) position is in the same Q range as the dis.-Cr_2AlC (100) plane.

The dis.-Cr_2AlC to Cr_2AlC transformation is finished at 801 °C, indicated by the disappearance of the dis.-Cr_2AlC (100) and (006) intensities and the appearance of Cr_2AlC (101), see Fig. 4c. In comparison to HPPMS-600, this temperature is in the same range as the start of the dis.-Cr_2AlC to Cr_2AlC formation for the former $(Cr,Al)_2C$ volumes.

The different formation temperatures between the coatings are related to both, the measurement and coating as-deposited state. Different coherent scattering volumes, the total amount of $(Cr,Al)_2C$ and amorphous phase, and the substrate to coating volume ratio – dependent on the sample adjustment in the P07 experiment – determine the detection limit of the formation start. If the reflection intensities of the coherent scattering volume of the newly formed phase are too low to overcome the background or overlapping other diffraction peaks at the beginning of the formation, this reaction will not be determinable. Therefore, the reaction may not be detected until a later time when the intensities increase due to the ongoing formation and the associated larger scattering volume. The dependency of the formation temperatures of dis.-Cr_2AlC on the initial phase is most likely related to short-range ordering of the amorphous phase. As discussed in the first paper of the series [12] for the formation of the $(Cr,Al)_2C$ phase in the as-deposited state, the possibility to form a unit cell as big as dis.-Cr_2AlC/Cr_2AlC is related to the available energy. Because of the short-range ordered amorphous phase, the energy necessary for dis.-Cr_2AlC formation is likely higher than the amount of energy needed if the initial phase has a very similar unit cell as $(Cr,Al)_2C$. Therefore the formation starting temperature is higher for the amorphous phase. The temperature dependence of the dis.-Cr_2AlC to Cr_2AlC transformation on the initial phase may be influenced by the texture of the $(Cr,Al)_2C$ phase. As reported by Gaudet et al. [26], the inheritance of texture between two phases can provide a lower energy pathway for phase formation. Hence, the observed texture inheritance for the $(Cr,Al)_2C$ to dis.-Cr_2AlC to Cr_2AlC formation (see Section 3.2.4) can reduce the formation temperature in comparison to the none-textured dis.-Cr_2AlC areas originate from the amorphous phase.

The Cr_2AlC formation route and temperatures for HPPMS-700 did not differ from HPPMS-600 and DCMS-600. Because the HPPMS-700 has a higher $(Cr,Al)_2C$ amount in the as-deposited state compared to HPPMS-600 (see Section 3.1), mostly the $(Cr,Al)_2C$ to dis.-Cr_2AlC formation is visible as for DCMS-600. While the formation start temperature for $(Cr,Al)_2C$ to dis.-Cr_2AlC was in the range of the HPPMS-600 coating, the Cr_2AlC finish temperature was in between DCMS-600 and HPPMS-600 at 815 °C (see Table 4 in Section 3.2.3).

The results for the WC–Co substrate – not shown in this paper – confirm the Cr_2AlC formation route and temperatures. There was no difference between WC–Co and IN718 substrates to be found.

3.2.1.2. Cr_2AlC phase formation – HT-XRD experiment. The HT-XRD results (Fig. 3d - Fig. 3f and Fig. 4d - Fig. 4f) provide a different view on the phase formation for the coatings because of the effect of the reflection geometry described above. As the result of the limited average information depth, the substrate intensities are very weak for both coatings. For DCMS-600, due to the strong texture of dis.-Cr_2AlC, the (103) reflection is not visible and $(Cr,Al)_2C$ (002), dis.-Cr_2AlC (006), and Cr_2AlC (006) show a very high intensity.

The results confirm the described Cr_2AlC formation route. However, due to the 140 min dwell time for each temperature step until 720 °C, the formation temperatures are significantly reduced compared to the temperatures determined in the P07 experiment. The DCMS-results in Fig. 4d to Fig. 4f reveal the start of the $(Cr,Al)_2C$ to dis.-Cr_2AlC formation at 500 °C. During the dwell time, the dis.-Cr_2AlC (002) intensity appears in form of a very broad hump and an increased shifting of the (100) and (006) diffraction peak is recognizable. Due to the overlapping of the $(Cr,Al)_2C$ (002) and dis.-Cr_2AlC (006) diffraction peak with the Pt (111) diffraction peak from the thermal couple, the start of this formation is not clearly visible for HPPMS-600 in Fig. 3d and Fig. 3f. However, the increased shifting of the dis.-Cr_2AlC (006) plane, as observed for DCMS-600, is visible during the 510 °C dwell time and may indicate the start of the $(Cr,Al)_2C$ to dis.-Cr_2AlC formation. As a result of the small coherent scattering volume of the $(Cr,Al)_2C$ phase and the lower resolution of the HT-XRD, it was not possible to detect the dis.-Cr_2AlC (002) plane before the amorphous to dis.-Cr_2AlC formation.

As for the P07 experiment, the amorphous to dis.-Cr_2AlC formation is only visible for HPPMS-600 and starts after the $(Cr,Al)_2C$ to dis.-Cr_2AlC formation. This formation occurs at 550 °C with the appearance of dis.-Cr_2AlC (002), (100), (006), and (103).

The dis.-Cr_2AlC to Cr_2AlC formation starts at 610 °C for DCMS-600 with weak intensities of Cr_2AlC (100), while for HPPMS-600 this occurs at 690 °C. Even though the start of the formation is about 80 K lower and 16 h later compared to the DCMS-600 coat-

ing, the finished Cr_2AlC formation is at a similar temperature of 710 °C and 720 °C for DCMS-600 and HPPMS-600, respectively. As described above for the P07 experiment, it is assumed that the $(Cr,Al)_2C$ phase and its texture inheritance decrease the dis.-Cr_2AlC and Cr_2AlC formation temperature. However, the relatively wide temperature and time range of 100 K and 20 h, where dis.-Cr_2AlC and Cr_2AlC both exist, is still in need of more detailed investigation.

The summary of the formation temperatures for the P07 and HT-XRD experiments is given in Table 4 in Section 3.2.3, with a comparison to the current literature.

3.2.2. Influence of disordering on the characteristic reflections of Cr_2AlC

In this section, a brief overview of the effect of a disordered state of the Cr_2AlC unit cell on the reflection intensities in the diffraction pattern and a brief comparison to the current literature state regarding the Cr_2AlC formation will be given.

In the current literature, the Cr_2AlC (002) and (101) planes are used to distinguish between the metastable phase in the intermediate state and Cr_2AlC [4,8,11,27]. This is appropriate if one assumes a smaller unit cell like $(Cr,Al)_2C$ or $(Cr,Al)_2C_x$ to be present in the intermediate state of the Cr_2AlC formation. The transformation of the intermediate phase to Cr_2AlC would be recognizable by the distinct shifting of the (002) and (101) diffraction peaks to lower Q values as the result of the increased lattice parameter c of Cr_2AlC compared to the small metastable phase [4,8,11,27]. However, by utilizing the high brilliance and energy of the P07 light source – resulting in increased peak to background ratio and enabling the measurement of very weak diffraction peaks – and the symmetric geometry for the X-ray reflection experiments, it was possible to detect the (002) reflection at Q = 9.5–9.6 nm^{-1} in the intermediate state. That indicates the presence of the large dis.-Cr_2AlC unit cell instead of $(Cr,Al)_2C$ or $(Cr,Al)_2C_x$. As discussed in Section 3.2.1, it was found that the dis.-Cr_2AlC (100), (006), and (103) reflections in the intermediate state show a pronounced shifting with increasing temperature, hence leading to the assumption of a disordered Cr_2AlC phase, where some positions in the unit cell are not occupied properly. The disordering increases the c/a ratio. During phase formation, the ratio decreases until the ordered state is reached.

The unit cells of the three different phases $(Cr,Al)_2C$, dis.-Cr_2AlC, and Cr_2AlC are shown in Fig. 5a, Fig. 5b, and Fig. 5c, respectively. They represent the three different crystalline stages of the Cr_2AlC formation. All three phases share the same hexagonal space group 194 ($P6_3/mmc$), where the C atoms are located at the Wyckoff position 2*a* (0,0,0) at the tetrahedral sites between the metal layer [9]. The occupancy of the C sites is 0.5 for $(Cr,Al)_2C$ and 1 for dis.-Cr_2AlC and Cr_2AlC [18,20]. In $(Cr,Al)_2C$, Cr and Al are randomly distributed at Wyckoff position 2*c* (1/3,2/3,1/4) [20]. In Cr_2AlC, the Cr atoms are located at Wyckoff position 4*f* (1/3,2/3,0.586) and the Al atoms at 2*c* (1/3,2/3,1/4) [18].

Zamulaeva et al. [10] found a similar disordered Cr_2AlC phase in coatings deposited by electrospark deposition. The difference in the lattice parameter was attributed to the disordering of the metal atoms [10].

In comparison to Cr_2AlC, the (002) reflection of dis.-Cr_2AlC is very weak and the (101) diffraction peak was not determinable over the whole intermediate state for the HPPMS-600 coating (Section 3.2.1). To investigate possible reasons, the influence of the Cr and Al positions in the Cr_2AlC unit cell were examined with the PowderCell software [28]. In Cr_2AlC, Al and Cr have distinct sites, whereas in $(Cr,Al)_2C$ both, Al and Cr occupy the same Cr positions. Likely, the ordering process for dis.-Cr_2AlC is mainly determined by Al and Cr occupying their sites in the unit cell – resulting in the lowest overall energy – during the intermediate state. The investigations revealed a stronger impact of the Al position on the (002) and (101) intensities. To investigate this effect and the c/a ratio over the course of the Cr_2AlC formation, the integrated P07 diffraction images of HPPMS-600 and DCMS-600 were analyzed by Rietveld refinement using the Match!3 software [17] with FullProf [29]. The Al z-position (z_{Al}) was used as a fit parameter because only z_{Al} shows the desired effect on the intensities. The atomic coordinates x_{Al} and y_{Al} were kept fixed to improve the fit. Because of the low intensities for the $(Cr,Al)_2C$ to dis.-Cr_2AlC formation in the case of HPPMS-600, this coating served as an example for the amorphous to dis.-Cr_2AlC formation, whereas DCMS-600 for the $(Cr,Al)_2C$ to dis.-Cr_2AlC formation. The results are summarized in Table 3 for $(Cr,Al)_2C$ at 500 °C, three temperatures referring to the start, middle, and end of the Cr_2AlC formation as well as Cr_2AlC at 25 °C after formation finished. Additionally, the calculated diffraction patterns in Fig. 5d give an idea of how the different z_{Al} positions influences the diffraction peak intensities, in particular for dis.-Cr_2AlC (002) and (101). As the calculated dis.-Cr_2AlC diffraction patterns show, only small changes, $\Delta z = \pm 0.005$, result in a noticeable decrease of the (002) intensity and the disappearance of the (101) diffraction peak.

The described influence of the disordered state on the (002) and (101) reflections intensity and the similarity between all three phases is apparent. The only distinguishing feature between $(Cr,Al)_2C$ and dis.-Cr_2AlC is the (002) reflection, whereas dis.-Cr_2AlC and Cr_2AlC are well distinguishable by the (006/103) splitting – resulting from the increased c/a-ratio – and the (101) reflection. Additionally, dis.-Cr_2AlC showed a pronounced broadening of (100) compared to $(Cr,Al)_2C$, which could be attributed to the disordering.

It has to be noted, that the given z_{Al} value for the dis.-Cr_2AlC is not equivalent to the actual position of the Al atoms in the unit cell. The disordered state should be understood as the occupation of the Cr_2AlC Al sites with slightly varying positions, as the hollowed Al in Fig. 5b indicates. As a result, the constructive interference is reduced and affected planes will show a decreased intensity and broader peak in the diffraction pattern – also decreasing the possibility to find those reflections. Additionally, the increasing dis.-Cr_2AlC (002) intensity in the intermediate state (see Section 3.2.1) can be interpreted as the increasing ordering of dis.-Cr_2AlC. Hence, the coherent volumes fulfilling the Bragg's equation for (002) increase because of the proper occupation of the Al sites in these volumes.

The lattice parameters of $(Cr,Al)_2C$, dis.-Cr_2AlC, and Cr_2AlC for HPPMS-600 and DCMS-600 and the c/a ratio show a distinctive trend, see Table 3. To compare the small $(Cr,Al)_2C$ unit cell to the large dis.-Cr_2AlC and Cr_2AlC unit cells, the values for three stacked $(Cr,Al)_2C$ unit cells are added. The relationship between $(Cr,Al)_2C$ and Cr_2AlC is apparent. Changing the stacking order of three stacked $(Cr,Al)_2C$ unit cells, by removing *C* atoms from this large unit cell at Wyckoff positions 4*e* (0,0,1/6), results in the Cr_2AlC unit cell [8].

Starting with a c/a ratio of 4.79, a = 2.815 Å, and $3 \cdot c$ = 13.47 Å for $(Cr,Al)_2C$ for HPPMS-600, during the Cr_2AlC formation, the decrease of the c/a ratio and c in combination with the increase of a was observed. The reduction in the unit cell c direction and increase in a is attributed to the ordering process of the Al and Cr atoms. While the c/a ratios and lattice parameter for $(Cr,Al)_2C$ and Cr_2AlC are similar for both coatings, the values for the start of the dis.-Cr_2AlC formation are different for HPPMS-600 and DCMS-600. The c/a ratio for DCMS-600 is significantly larger and closer to $(Cr,Al)_2C$. The influence of the different formation temperature on the ratios can be excluded because no noticeable differences were observed for Cr_2AlC at different temperatures for both coatings. Additionally, the ratio for DCMS-600 at 708 °C is

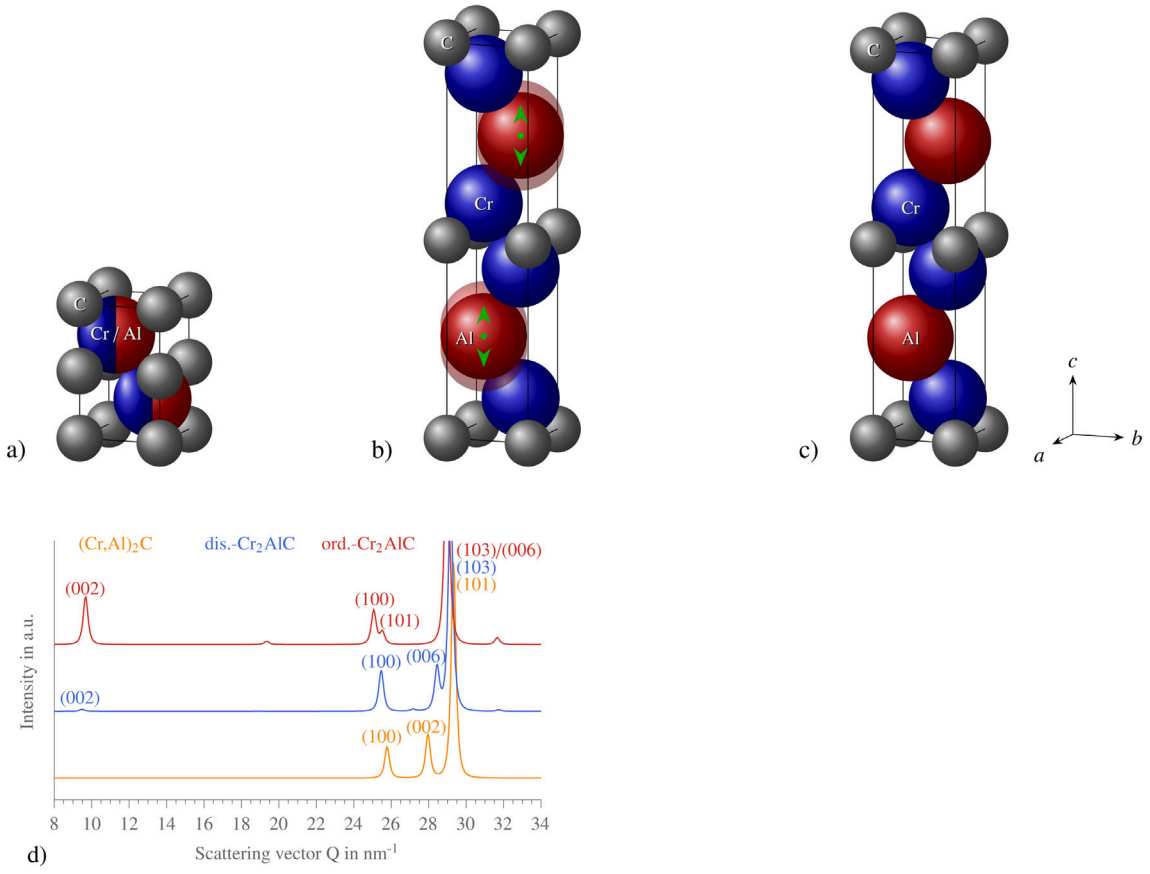

Fig. 5. Unit cells of a) $(Cr,Al)_2C$ at 500 °C (note that the occupancy of the C sites 2a is 0.5), b) dis.-Cr_2AlC at 757 °C and c) Cr_2AlC at 843 °C, with the corresponding diffraction pattern in d). The used lattice parameter and the z_{Al} value of dis.-Cr_2AlC is summarized in Table 3. The diffraction patterns were calculated with the MATCH!3 software [17] on basis of the Rietveld refinement results of the HPPMS-600 coating at the given temperatures.

Table 3
Lattice parameter of $(Cr,Al)_2C$, dis.-Cr_2AlC and Cr_2AlC phases over the course of the Cr_2AlC formation for HPPMS-600 and DCMS-600 coatings, calculated by Rietveld refinement using the Match!3 software [17] with FullProf [29]. The uncertainties of $\pm 6{\cdot}10^{-3}$ Å for a and $\pm 2{\cdot}10^{-2}$ Å for c were calculated from the detector resolution limit.

Coating	Temperature	Phase	a in Å	c in Å	c/a ratio	z_{Al}
HPPMS-600	500 °C	$(Cr,Al)_2C$	2.815	4.49 3 · c= 13.47	1.60 (3 · c)/a = 4.79	-
	677 °C	dis.-Cr_2AlC	2.845	13.29	4.67	0.245
	757 °C	dis.-Cr_2AlC	2.852	13.26	4.65	0.245
	843 °C	Cr_2AlC	2.895	13.00	4.49	0.25
	25 °C	Cr_2AlC	2.865	12.85	4.49	0.25
DCMS-600	500 °C	$(Cr,Al)_2C$	2.817	4.48 3 · c= 13.44	1.59 (3 · c)/a = 4.77	-
	628 °C	dis.-Cr_2AlC	2.826	13.35	4.72	0.245
	708 °C	dis.-Cr_2AlC	2.849	13.19	4.63	0.247
	801 °C	Cr_2AlC	2.892	13.00	4.50	0.25
	25 °C	Cr_2AlC	2.864	12.84	4.48	0.25

smaller than that for HPPMS-600 at 757 °C. This finding supports the theory that the $(Cr,Al)_2C$ to dis.-Cr_2AlC formation requires less thermal energy than the amorphous to dis.-Cr_2AlC formation because of the structural similarities of $(Cr,Al)_2C$ and dis.-Cr_2AlC, as discussed in Section 3.2.1. However, because the amorphous to dis.-Cr_2AlC formation occurs without the restrictions of an existing unit cell, the lattice parameter and thereby the c/a ratio of dis.-Cr_2AlC is closer to Cr_2AlC.

The results for the Cr_2AlC lattice parameter and c/a-ratios at 25 °C are in good agreement with the literature [4,8,11,27].

Besides the different intermediate phases found in this study and the literature, the $(Cr,Al)_2C$ phase in the as-deposited state and the description of the Cr_2AlC formation process with one intermediate phase is in accordance with the current literature [4,8,11,27]. The theoretical evaluation in this section and the results in Section 3.2.1 clearly show the difficulties for the analysis of the intermediate phase by X-ray diffraction techniques – usually used for Cr_2AlC PVD-coating phase identification [4,8,11,27].

In difference to this investigation, the grazing incidence geometry was used in [4,11,27] to avoid strong substrate diffraction peak overlapping, which is known for increased reflection broadening in particular for low Q-values. Therefore, the very weak diffraction peaks may be hidden in the background. Additionally, all these investigations started with pure amorphous coatings. As discussed in Section 3.2.1, the presence of textured $(Cr,Al)_2C$ in the as-deposited state, leading to the increased dis.-Cr_2AlC (002) intensities in the 90° azimuth direction in the intermediate state, facilitate the detection of this diffraction peak. Additionally, the possibility to investigate different as-deposited states (see Section 3.1) also improved the understanding of the Cr_2AlC formation.

The investigations in [4,8,11,27] were performed ex-situ. As shown in Fig. 3h, the dis.-Cr_2AlC (002) intensity increase is tied to a narrow temperature and time range. It could be challenging to find this range before the dis.-Cr_2AlC to Cr_2AlC formation.

It has to be noted, that besides X-ray diffraction, transmission electron microscopy (TEM) and high-resolution TEM (HRTEM) [4,11,27], Raman spectroscopy [4], and electrical resistivity measurements [11] were used to evaluate phase formation and formation temperatures. While TEM-investigations as a special diffraction technique face similar difficulties regarding the distinction between $(Cr,Al)_2C$ and dis.-Cr_2AlC as described earlier, Raman spectroscopy and electrical resistivity measurements can be used to improve the accuracy of the temperature range for the formation. As described in [4,11], both measurement techniques are sensitive to disordering in unit cells [4,11], which is the case for $(Cr,Al)_2C_x$ and dis.-Cr_2AlC.

It can be concluded, that the X-ray diffraction results in the literature do not show the dis.-Cr_2AlC (002) diffraction peak, which is the important feature for the distinction between $(Cr,Al)_2C$ and dis.-Cr_2AlC. However, the absence of dis.-Cr_2AlC (002) may result from experimental or characterization difficulties and the results in [4,8,11,27] show the same tendencies for the diffraction peaks, like the shifting of dis.-Cr_2AlC/$(Cr,Al)_2C$ (100), (006), (103), and missing (101), as described in this work. The detailed discussion that dis.-Cr_2AlC may be found in the results of the described papers is given in Section 3.2.3. The results in this section and Section 3.2.1 clearly show the formation of the same intermediate phase from amorphous phase and $(Cr,Al)_2C$ during heat treatment. The presence and increase of the (002) diffraction peak for *Q*-values at about 9.6 nm^{-1} in the intermediate state, the disappearance of the $(Cr,Al)_2C$ (002) during the intermediate state, and the broadening of the former $(Cr,Al)_2C$ (100) reflection with the start of the intermediate state for the DCMS-600 coating (see Section 3.2.1) support the assumption of dis.-Cr_2AlC as the intermediate phase.

3.2.3. Comparison of the Cr_2AlC formation temperatures to the literature state

The formation temperatures for the intermediate state and Cr_2AlC are given in Table 4 and will be discussed regarding the current literature state in this section. As described in Section 3.2.2, the intermediate phase from the literature is different from dis.-Cr_2AlC, which is found in this study. However, as discussed in Section 3.2.2, it is assumed that the intermediate phase was not described correctly in the literature for given reasons and the comparison of the formation temperatures for the intermediate state is reasonable. Therefore the formation temperatures from the literature are assigned to the amorphous to dis.-Cr_2AlC formation.

The formation temperatures in Table 4 reported by Abdulkadhim et al. [8] and Zhang et al. [27] refer to the reaction peak temperature obtained by DSC measurement, while the formation temperatures reported by Stelzer et al. [11] originate from in situ TEM measurements. As described earlier for the diffraction experiments, in order to determine the start of the phase formation by XRD, a sufficient coherent volume is necessary. Thereby the temperatures may differ in dependence on the measurement method. Therefore the whole formation range from the first to the last determinable signal is given in Table 4 for the three formation reactions, if applicable.

The formation temperature for the reaction amorphous to dis.-Cr_2AlC is in good agreement with the literature for the HT-XRD experiment for HPPMS-600. Considering the influence of the heating rate and the different measurement strategies, the increased formation temperature for the P07 experiment for HPPMS-600 is still comparable.

For the second reaction dis.-Cr_2AlC to Cr_2AlC, the results from the literature are only comparable to the formation onset temperatures of DCMS-600. However, as described in Section 3.2.1, the formation temperature for the DCMS-600 coating refers to the formation where $(Cr,Al)_2C$ is the initial phase in the as-deposited state, which was found to be lower compared to the amorphous phase in the case of HPPMS-600. Therefore the formation temperature difference with an amorphous phase in the as-deposited state is in the range of 50 K to 100 K compared to the literature. Different influences may cause the deviation, but the respective individual impact could not be clarified. One possible reason could be the sputter process, where wide property ranges are possible and thereby varying formation temperatures can occur. That can be seen in the results of the P07 experiments. Stelzer et al. [11] showed that furthermore sample size, temperature control, and measurement method have an impact on the results of in situ TEM and ex-situ XRD experiments. The high spatial resolution in combination with the small sample size, needed for TEM or DSC measurements, can increase the possibility of finding the formation start in small areas of the sample. As in the larger used samples for XRD measurements, the reactions have to happen in larger coherent areas to be determinable against the background. Additionally, temperature is sometimes an uncertainty and can not always be controlled properly. While the P07 experiments were performed with a dilatometer with high time and temperature accuracy, possible temperature deviations for the HT-XRD dome are not assessable. To achieve the highest possible accuracy, a thermal couple was point welded on the sample surface. The 10 mm x 10 mm x 1 mm sample is held by two unheated alumina rods and the resistant heater is placed at the bottom of the sample. Due to the sample positioning and water cooling of the chamber, high unknown temperature gradients over the sample are possible. This effect intensifies when chamber temperatures are increasing and could cause temperature variations compared to other measurement methods.

Besides the discussed literature sources, Ougier et al. [4] and Tang et al. [30] reported very low Cr_2AlC formation temperatures in the range of 500 °C. A careful review of the results in [4] allows

Table 4
Formation temperatures and temperature ranges for the amorphous/$(Cr,Al)_2C$ to dis.-Cr_2AlC and the dis.-Cr_2AlC to Cr_2AlC formation for the DCMS-600, HPPMS-700 and HPPMS-600 coatings for the P07 and HT-XRD experiments. Formation temperatures of in situ investigations from the literature are added for comparison. The amorphous/$(Cr,Al)_2C$ to dis.-Cr_2AlC formation is comparable with the amorphous to $(Cr,Al)_2C$/$(Cr,Al)_2C_x$ formation in the literature. The formation temperature in the brackets is an assumption due to diffraction peak overlapping (see Section 3.2.1).

	Coating	$(Cr,Al)_2C \rightarrow$ dis.-Cr_2AlC	amorph. $\rightarrow$ dis.-Cr_2AlC	dis.-$Cr_2AlC \rightarrow Cr_2AlC$
P07 30 K/min	DCMS-600	609 °C - 628 °C	-	695 °C - 801 °C
	HPPMS-600	632 °C	677 °C	804 °C - 843 °C
	HPPMS-700	634 °C	-	762 °C - 815 °C
HT-XRD 2 h dwell time	DCMS-600	500 °C	-	610 °C - 710 °C
	HPPMS-600	(510 °C)	550 °C	690 °C - 720 °C
[11] 5 K/min	DCMS	-	564 °C - 567 °C	591 °C - 594 °C
[8] 10 K/min	DCMS	-	570 °C	610 °C
[27] 20 K/min	DCMS	-	595 °C	640 °C

the assumption that the phase at 500 °C and 550 °C was dis.-Cr_2AlC instead of Cr_2AlC. Ougier et al. [4] reported the decrease of the *c* lattice parameter for these temperatures compared to the results for 600 °C similar to the observation discussed in Section 3.2.2 for dis.-Cr_2AlC. Additionlly, the diffraction patterns for 500 °C and 550 °C show the dis.-Cr_2AlC (006)/(103) splitting. The splitting decreases from a possible separate (006) intensity at around 2θ = 40° for 500 °C to a shoulder at the (103) diffraction peak at around 2θ = 42° for 550 °C. Additionally, the Raman spectroscopy results show a difference between 500 °C and 550 °C compared to 600 °C. The 1a peak, which is usually a sign of improved crystallinity [4], was first determinable at 600 °C. According to Barsoum et al. [31], this 1a peak or ω_1 mode represents the movement of Al and Cr in the direction parallel to the unit cell basal plane. The ω_3 (1c in [4]) and ω_4 (1d in [4]) modes, which are visible in the spectroscopy results, represent only the Cr atom movement. These findings support the assumption of the shifted Al-atoms for dis.-Cr_2AlC discussed in Section 3.2.2. Nevertheless, the results from Qugier et al. [4] show that the formation temperature of the amorphous to dis.-Cr_2AlC reaction could be lower for very long dwell times and in the range of the $(Cr,Al)_2C$ to dis.-Cr_2AlC formation as reported in this study.

Tang et al. [30] reported a Cr_2AlC formation temperature of 500 °C. They used Cr, Al, and C elemental layers, which may reduce the formation temperature as observed for $(Cr,Al)_2C$ as the initial phase compared to the amorphous phase. Additionally, a pronounced (002) texture impedes the investigation of a possible broad dis.-Cr_2AlC (100) diffraction peak to Cr_2AlC (100)/(101) transition, as an additional feature for the two different phases. The Cr_2AlC (002) intensity increase in [30] shows some similarity to those in this study, which could be a hint to an intermediate phase formation, which would be in good agreement with the HT-XRD results in this study.

3.2.4. Texture and texture inheritance during Cr_2AlC phase formation

The investigated coatings showed a unique texture inheritance during the Cr_2AlC formation for the initial $(Cr,Al)_2C$ volumes. The texture interpretation will be discussed on heat maps showing the azimuth dependence of the characteristic reflections in *Q* range of 24.5 nm^{-1} to 30.5 nm^{-1}.

The determination of whole pole figures or ODF presentation was not possible during the P07 experiments, because the sample geometry and the experiment installment did not allow the rotation about the sample surface normal. PVD coatings often show a fiber texture, where a particular crystallographic axis aligns with the surface normal, which was determined with the experimental setup [32, p. 228]. However, the distribution of crystallographic directions about the fiber axis (surface normal) was not determinable. While the measurement of the rotation about the fiber axis is necessary for the calculation of ODF representation, it is not mandatory for the interpretation of the fiber texture if the azimuth dependence in transmission geometry is available.

Fig. 6 summarizes the azimuth dependence of the three characteristic reflections of $(Cr,Al)_2C$, dis.-Cr_2AlC and Cr_2AlC for the HPPMS-600 (Fig. 6a - Fig. 6c), HPPMS-700 (Fig. 6d - Fig. 6f), and DCMS-600 (Fig. 6g - Fig. 6i) coatings. The left images represent the $(Cr,Al)_2C$ phase at 600 °C before the formation start, the images in the middle the intermediate state with dis.-Cr_2AlC and the right images the Cr_2AlC phase at 843 °C for the respective coating. The *Q* dependence of the reflections on the azimuth direction is related to residual stress and is discussed in the first paper of the series [12].

Fig. 6a, Fig. 6d, and Fig. 6g show the distinct $(Cr,Al)_2C$ (002) texture, with the local intensity maxima in nearly the 90° and 270° azimuth direction. The *c* axis is thereby parallel to the sample surface normal and the (002) plane parallel to the sample surface. A minor tilt of the fiber axis could be attributed to a sample rotation in the experiment, or the coating process as the result of an inclined sputtered flux during the coating process. The maxima for the $(Cr,Al)_2C$ (101) reflection are located at azimuth angle about 30°/ 150°/ 210°/ 330° with an angle of about 60° to the (002) plane. This angular relation gives additional evidence for $(Cr,Al)_2C$ or a structural equivalent hexagonal phase in the as-deposited state. The texture is in particular recognizable for the DMCS-600 coating because of the highest amount of $(Cr,Al)_2C$, as discussed earlier.

As described in Section 3.2.1, two different dis.-Cr_2AlC phases are detectable during the intermediate state. This correlation is in particular recognizable for the HPPMS-600 coating in Fig. 6b. The $(Cr,Al)_2C$ texture inherits to dis.-Cr_2AlC, resulting in the dis.-Cr_2AlC (006) intensity maxima at the same azimuth angles as $(Cr,Al)_2C$ (002). In contrast, the volumes originating from the amorphous phase do not show any distinct texture, visible by a continuous dis.-Cr_2AlC (006) intensity at slightly higher *Q* values.

The texture inheritance from $(Cr,Al)_2C$ to dis.-Cr_2AlC to Cr_2AlC is well observable for the DCMS-600 coating. All three images (Fig. 6g - Fig. 6i) show the intensity maxima of the (006) and (103) reflections for $(Cr,Al)_2C$, dis.-Cr_2AlC, and Cr_2AlC at the same azimuth angles. Even the Cr_2AlC (006)/(103) doublet, for which the two reflections are not distinguishable, can be recognized by the local maxima from the texture. The intensity maxima for the (006)/(103) doublet are only marginally detectable for HPPMS-700 and not noticeable for HPPMS-600 because of the higher Cr_2AlC amount originating from amorphous areas. As discussed in Section 3.2.1, the inheritance of the texture can lead to the decrease of the required thermal energy for phase formation.

The texture inheritance results in a different texture of Cr_2AlC, if the Cr_2AlC formation occurs during a annealing post-treatment – like the in situ P07 experiments – with $(Cr,Al)_2C$ in the as-deposited state compared to coatings where the Cr_2AlC formation occurs during the deposition process. As reported in the literature, if Cr_2AlC forms during the deposition process, the coatings often show a (110) texture because of the energetically more favorable grow direction along the smaller *a*/*b* axis compared to the larger *c* axis [33,34].

The different texture of $(Cr,Al)_2C$ and Cr_2AlC in the coating process is related to the *c*/*a* ratio. The basal plane is often characterized by the lowest surface energy [35]. Therefore, if the kinetic energy of the sputtered flux and the thermal energy at the sample surface, provided by the deposition process, are sufficient for the phase formation but too low for high atom mobility at the sample surface and whereby only nuclei with the plane with the lowest surface energy sufficiently aligned to the direction of the sputtered flux can grow, formation of a texture will occur. However, the texture may change in dependence on deposition parameters and coating thickness. The texture of hexagonal unit cells depends on the *c*/*a* ratio. If the ratio is below the value of 1.63, which is the case for $(Cr,Al)_2C$ with ≈ 1.60 (see Table 3), the preferred growing direction is along the *c* axis resulting in a preferential orientation of the (002) plane perpendicular to the surface. If the ratio exceeds this value, which is the case for Cr_2AlC with ≈ 4.49. (Table 3), the texture changes to (110). [33,35,36,37].

3.2.5. Influence of the deposition process on the phase composition after Cr_2AlC phase formation

In this section, the influence of the deposition process on the phase composition after the finished Cr_2AlC formation is discussed. As described in Section 3.1 and the first paper of the series [12], the Cr/Al ratio is increased for the amorphous areas and the HPPMS coatings in the as-deposited state (see Fig. 2 and Table 2 in Section 3.1). The preferred Al resputtering in the HPPMS process and the amorphous phase – resulting from the higher kinetic energy of the sputtered flux compared to DCMS and from the different

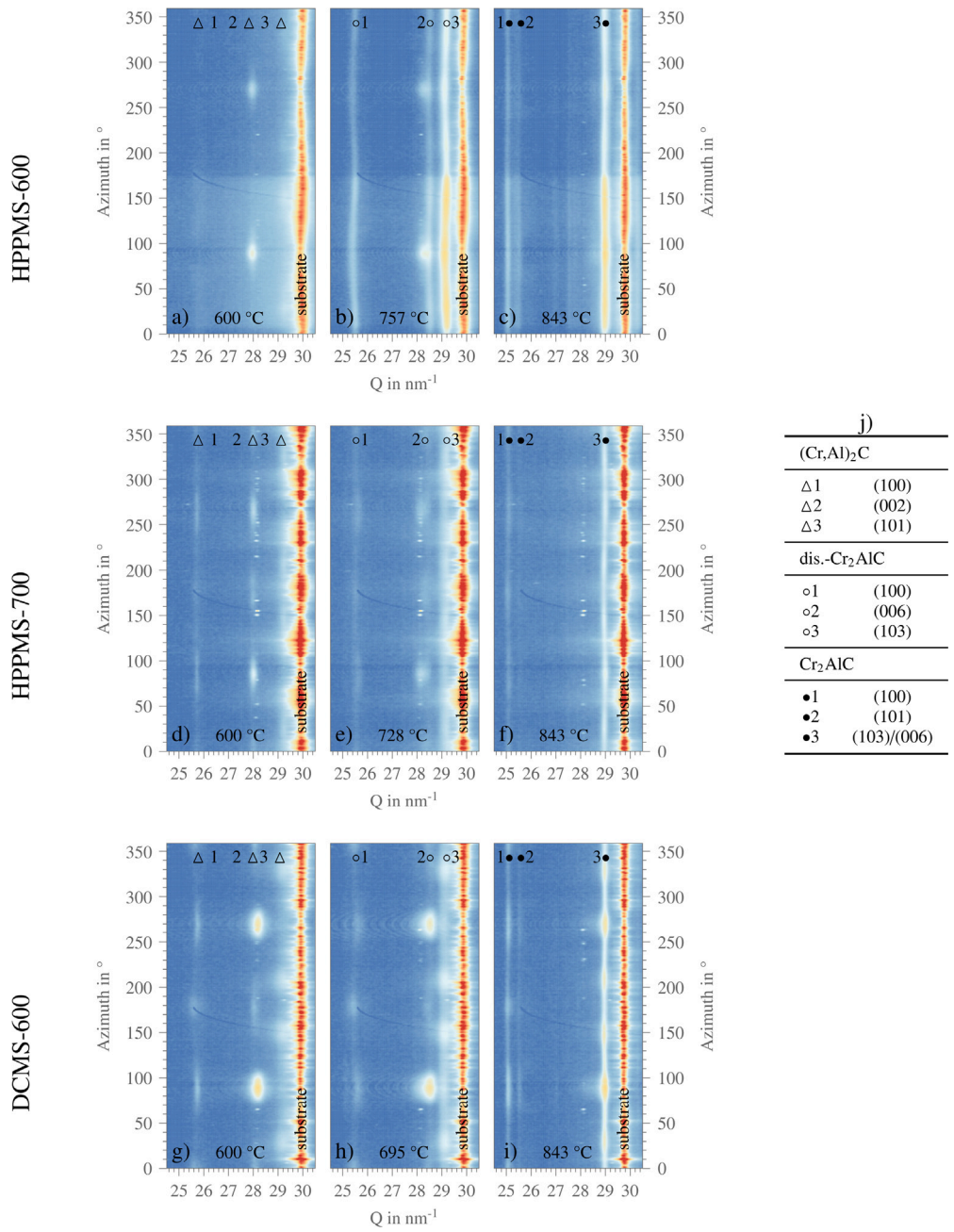

Fig. 6. Q-azimuth heat maps for HPPMS-600 (a)-(c), HPPMS-700 (d)-(f), and DCMS-600 (g)-(i) obtained by P07 experiments. (a), (d), (g) show the coatings before the dis.-Cr_2AlC formation at 600 °C. (b), (e), (h) show HPPMS-600 at 757 °C, HPPMS-700 at 728 °C, and DCMS-600 at 695 °C. (c), (f), (i) show the coatings at 843 °C after the Cr_2AlC formation. j) summarizes the reflections marked in (a) - (i).

Al bonding in the amorphous phase compared to $(Cr,Al)_2C$, respectively – was assumed to be the reason for this phenomena.

Fig. 7 shows the cross-section of the HPPMS-600, HPPMS-700 and DCMS-600 coatings after the finished Cr_2AlC formation during an annealing post-treatment at 800 °C with 1 h dwell time. Area 1 and Area 2 correspond to the former $(Cr,Al)_2C$ and amorphous areas in Fig. 2 (Section 3.1), respectively. In accordance to the results in Section 3.2.1, Cr_2AlC and Cr_7C_3 were identified as the two phases in both areas by surface X-ray diffraction in reflection geometry and cross-section EDS analysis.

In order to determine the Cr_2AlC and Cr_7C_3 quantities for the two areas and the three coatings, an image analysis approach, using the Fiji-ImageJ software with the Trainable Weka Segmentation Plugin [38,39], was carried out. Considering the analysis approach and a possible influence of the location of the cross-section images for Area 1, which shows slightly different Cr_7C_3 concentrations for different image parts, the maximum error for this approach is estimated to be ±5 %.

In Table 5 the estimated fractions of Cr_2AlC and Cr_7C_3 for the two areas for the HPPMS-600, HPPMS-700 and DCMS-600 coatings are summarized. The results confirm a higher Cr_7C_3 amount for the HPPMS coatings and Area 2, compared to Area 1 of the respective coating, for all three coatings resulting from the higher Cr content. A sufficient accuracy of the used analysis approach is confirmed by the similar Cr_2AlC and Cr_7C_3 amounts in Area 1 of the HPPMS-600 and Area 2 of DCMS for which a similar Cr and Al concentration was determined (see Section 3.1). The thin Cr_7C_3 surface layer – in particular visible for DCMS-600 in Fig. 7c – was excluded from

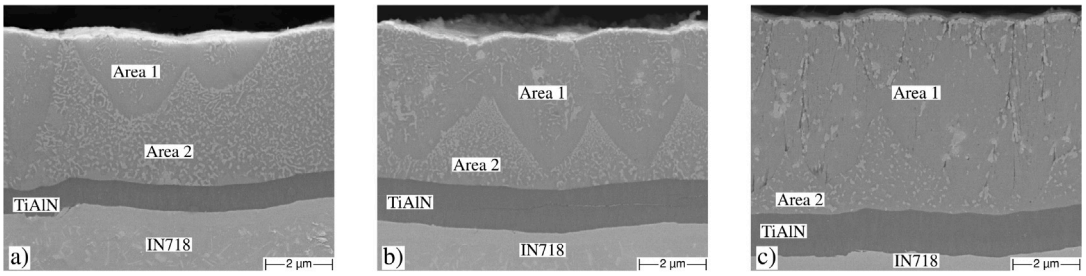

Fig. 7. SEM cross-section images of ground (a) HPPMS-600, (b) HPPMS-700 and (c) DCMS-600 coatings with TiAlN interdiffusion barrier on IN718 substrate after heat treatment at 800 °C for 1 h dwell time. (from the first paper of the series [12]).

Table 5
Average Cr_2AlC and Cr_7C_3 amounts for the two areas in Fig. 7 for HPPMS-600, HPPMS-700 and DCMS-600 coatings after heat treatment at 800 °C for 1 h dwell time. Values were determined by analysis of SEM cross-section images using the Fiji-ImageJ software with the Trainable Weka Segmentation Plugin [38,39]. The error is estimated ±5 %. (from the first paper of the series [12]).

	HPPMS-600		HPPMS-700		DCMS-600	
	Area 1	Area 2	Area 1	Area 2	Area 1	Area 2
Cr_2AlC in vol%	88	62	77	64	91	86
Cr_7C_3 in vol%	12	38	23	36	9	14

the analysis for any coating. Those layers are the result of the surface oxidation, associated with the formation of an alumina layer and thereby the near-surface aluminum depletion. Additionally, the Cr_7C_3 at the wide column boundaries for DCMS-600 may originate from oxygen migration and the subsequent oxidation of Cr_2AlC. Therefore the Cr_7C_3 content could be lower.

The estimated Cr_7C_3 amounts follow the Cr content trends from the EDS measurements of the as-deposited state. The highest Cr content in Area 1 for HPPMS-700 (68.9 at.%) among the three coatings resulted in the highest Cr_7C_3 amount of 23 %. The former amorphous areas of the two HPPMS coatings are characterized by the highest Cr_7C_3 content of 36–38 %.

Besides the different Cr_7C_3 quantities in the two areas, differences in grain size and distribution are apparent. While fine-grained Cr_7C_3 in Area 2 is more uniformly distributed, Area 1 is characterized by large and small located Cr_7C_3 grains. Additionally, the edges of Area 1 in the case of the HPPMS coatings show decreased Cr_7C_3 quantities and the adjacent edges of Area 2 increased Cr_7C_3 amounts. These microstructure features could result from the annealing post-treatment and deposition process. However, it was not possible to associate these effects exclusively to one of the two origins.

According to Mertens et al. [2], single-phase Cr_2AlC coatings were deposited in the elemental composition ranges $1.42 < Cr/Al < 2.03$ and $1.72 < Cr/C < 1.93$. However, while the Cr/Al ratios of the DCMS-600 coating is in the range for the Cr_2AlC single-phase, it was not possible to determine the C content with sufficient accuracy because of the usually high error for low-Z elements for EDS analysis and the necessity of a carbon deposition for the cross-section SEM investigations. Additionally, the composition ratios in [2] were determined for sputtered coatings, while the annealing post-treatment treatment in this investigation is more likely comparable to the Cr-Al-C phase diagram, with a very small area of existence for Cr_2AlC. According to the isothermal section of the Cr-Al-C ternary phase diagram at 800 °C [40], an increased Cr content results in the Cr_2AlC, Cr_7C_3, and Cr_2Al phase field. However, comparable to other studies [6,41], only Cr_2AlC and Cr_7C_3 were determinable and no evidence for Cr_2Al was found. Because the C content could not be determined with sufficient accuracy, the estimation of the Cr_7C_3 quantity on basis of the isothermal section and evalutation of the results in this study is not reasonable.

4. Conclusion

This paper is dedicated to the investigation of the Cr_2AlC formation route with amorphous Cr-Al-C and $(Cr,Al)_2C$ as initial phases in the as-deposited state. In particular, the in-depth description of the intermediate phase and the discussion of the new results in comparison to the current literature state are carried out. The influence of the deposition process on the Cr_2AlC formation, texture, and phase composition is considered and their respective influence discussed.

Cr-Al-C coatings were deposited by the HPPMS and DCMS processes, with the variation of the deposition temperature on IN718 and WC–Co substrates. In-situ heat treatment synchrotron experiments were used to investigate the Cr_2AlC phase formation, utilizing the high brilliance and energy of the beamline P07 for phase identification and description. Furthermore, in situ HT-XRD experiments for the determination of the formation temperatures with a 140 min dwell time for each temperature step were carried out. Electron microscopy was used for the investigation of the phase composition after Cr_2AlC phase formation.

From the results of the P07 and HT-XRD experiments, the following Cr_2AlC formation route for amorphous Cr-Al-C and metastable $(Cr,Al)_2C$ coatings is proposed.

Additionally it was found, that.

- Cr_2AlC has at least two different metastable phases – $(Cr,Al)_2C$ and dis.-Cr_2AlC,
- $(Cr,Al)_2C$ is a metastable phase in the as-deposited state, but is not formed during the Cr_2AlC formation by heat treatment,
- dis.-Cr_2AlC is the intermediate phase for the Cr_2AlC phase formation during heat treatment, characterized by an ordering process with increasing temperature and time,
- the formation is diffusion controlled.

Dis.-Cr_2AlC is the intermediate phase with a similar unit cell as Cr_2AlC but increased c and decreased a lattice parameter, as the result of a disordered state. It is assumed that in particular the occupation of Cr_2AlC Al sites contribute to the disordered state and ordering process during the dis.-Cr_2AlC to Cr_2AlC formation process. The c/a ratio was found to continuously decrease during the phase formation from $(Cr,Al)_2C$ to Cr_2AlC.

The formation temperature of dis.-Cr_2AlC and Cr_2AlC were found to depend on the initial phase, with a decreased formation temperature for $(Cr,Al)_2C$, and the deposition process. The DCMS coating showed the lowest formation temperature for dis.-Cr_2AlC and Cr_2AlC during the synchrotron experiments with constant heating rate, while the formation temperatures during the heat treatment with 2 h dwell time showed similar formation temperatures for both coatings– except the dis.-Cr_2AlC to Cr_2AlC start temperature for the DCMS coating being lower.

The dis.-Cr_2AlC and Cr_2AlC phase showed a pronounced (002) fiber texture if the initial phase was $(Cr,Al)_2C$, as the result of the texture inheritance. Additionally, the texture can decrease the formation start temperatures for the $(Cr,Al)_2C$ to Cr_2AlC formation route in comparison to the amorphous origin.

The final coatings after the Cr_2AlC formation consisted of mainly Cr_2AlC and Cr_7C_3. The Cr_7C_3 content was found to depend on the deposition process, hence the Cr content in the as-deposited state and was increased for the HPPMS coatings and the amorphous volumes.

Despite the in-depth description of the Cr_2AlC phase formation for the two different initial phases with the dis.-Cr_2AlC phase, the influence of the coating process on the formation temperatures and microstructure of the coatings after the phase formation, and some aspects regarding texture phenomena, this work has also raised new questions. In particular, the possibility of different ordering states of dis.-Cr_2AlC in dependence on the initial phase and the partly wide formation range are still in need for further investigation.

Declaration of competing interest

The authors declare that they have no known competing financial interests or personal relationships that could have appeared to influence the work reported in this paper.

Data availability

Data will be made available on request.

Acknowledgements

Max Thorhauer is thanked for the great help and time during the experiments at DESY. Mirko Heckert is acknowledged for the helpful proofreading and discussion.

Funding

This work was supported by the Deutsche Forschungsgemeinschaft (DFG) [Grant No. LE1373/41–1]; and Deutsche Elektronen und Synchrotron (DESY) [proposal I-20180296].

References

[1] J.M. Schneider, Z. Sun, R. Mertens, F. Uestel, R. Ahuja, Ab initio calculations and experimental determination of the structure of Cr2AlC, Solid State Commun. 130 (7) (2004) 445–449, https://doi.org/10.1016/j.ssc.2004.02.047.
[2] R. Mertens, Z. Sun, D. Music, J. Schneider, Effect of the composition on the structure of Cr-Al-C investigated by combinatorial thin film synthesis and ab initio calculations, Adv. Eng. Mater. 6 (11) (2004) 903–907, https://doi.org/10.1002/adem.200400096.
[3] P. Eklund, M. Beckers, U. Jansson, H. Högberg, L. Hultman, The Mn+1AXn phases: Materials science and thin-film processing, Thin Solid Films 518 (8) (2010) 1851–1878, https://doi.org/10.1016/j.tsf.2009.07.184.
[4] M. Ougier, A. Michau, F. Lomello, F. Schuster, H. Maskrot, M.L. Schlegel, High-temperature oxidation behavior of HiPIMS as-deposited Cr–Al–C and annealed Cr2AlC coatings on Zr-based alloy, J. Nucl. Mater. 528 (2020) 151855, https://doi.org/10.1016/j.jnucmat.2019.151855.
[5] K. Sarakinos, J. Alami, S. Konstantinidis, High power pulsed magnetron sputtering: A review on scientific and engineering state of the art, Surf. Coat. Technol. 204 (11) (2010) 1661–1684, https://doi.org/10.1016/j.surfcoat.2009.11.013.
[6] D. Shtansky, P. Kiryukhantsev-Korneev, A. Sheveyko, B. Mavrin, C. Rojas, A. Fernandez, E. Levashov, Comparative investigation of TiAlC(N), TiCrAlC(N), and CrAlC(N) coatings deposited by sputtering of MAX-phase Ti2-xCrxAlC targets, Surf. Coat. Technol. 203 (23) (2009) 3595–3609, https://doi.org/10.1016/j.surfcoat.2009.05.036.
[7] C. Walter, D.P. Sigumonrong, T. El-Raghy, J.M. Schneider, Towards large area deposition of Cr2AlC on steel, Thin Solid Films 515 (2) (2006) 389–393, https://doi.org/10.1016/j.tsf.2005.12.219.
[8] A. Abdulkadhim, M. to Baben, T. Takahashi, V. Schnabel, M. Hans, C. Polzer, P. Polcik, J.M. Schneider, Crystallization kinetics of amorphous Cr2AlC thin films, Surface and Coatings Technology 206 (4) (2011) 599–603. doi:10.1016/j.surfcoat.2011.06.003.
[9] S.M. Schmuecker, D. Clouser, T.J. Kraus, B.M. Leonard, Synthesis of metastable chromium carbide nanomaterials and their electrocatalytic activity for the hydrogen evolution reaction, Dalton Trans. 46 (39) (2017) 13524–13530, https://doi.org/10.1039/C7DT01404J.
[10] E.I. Zamulaeva, E.A. Levashov, T.A. Sviridova, N.V. Shvyndina, M.I. Petrzhik, Pulsed electrospark deposition of MAX phase Cr2AlC based coatings on titanium alloy, Surf. Coat. Technol. 235 (2013) 454–460, https://doi.org/10.1016/j.surfcoat.2013.08.002.
[11] B. Stelzer, X. Chen, P. Bliem, M. Hans, B. Völker, R. Sahu, C. Scheu, D. Primetzhofer, J.M. Schneider, Remote tracking of phase changes in Cr2AlC thin films by in-situ resistivity measurements, Scient. Rep. 9 (1) (2019) 8266, https://doi.org/10.1038/s41598-019-44692-4.
[12] S. Heinze, T. Krülle, L. Ewenz, C. Krywka, A. Davydok, A. Stark, R. Cremer, C. Leyens, Influence of the deposition process and substrate on microstructure, phase composition, and residual stress state on as-deposited Cr-Al-C coatings, SSRN Electronic J. (2022), https://doi.org/10.2139/ssrn.4163387.
[13] HAYNES 718 alloy brochure, http://haynesintl.com/docs/default-source/pdfs/new-alloy-brochures/high-temperature-alloys/brochures/718-brochure.pdf?sfvrsn=14, (accessed 15 June 2022) (2022).
[14] N. Schell, A. King, F. Beckmann, T. Fischer, M. Müller, A. Schreyer, The high energy materials science beamline (HEMS) at PETRA III, Mater. Sci. Forum 772 (2013) 57–61, https://doi.org/10.4028/www.scientific.net/MSF.772.57.
[15] A.P. Hammersley, FIT2D: An introduction and overview, Tech. Rep. ESRF97HA02T (1997).
[16] A.P. Hammersley, S.O. Svensson, M. Hanfland, A.N. Fitch, D. Hausermann, Two-dimensional detector software: From real detector to idealised image or two-theta scan, High Press. Res. 14 (4–6) (1996) 235–248, https://doi.org/10.1080/08957959608201408.
[17] Match! - Phase Analysis using Powder Diffraction, Dr. H. Putz & Dr. K. Brandenburg GbR.
[18] Cr2AlC crystal structure: Datasheet from "PAULING FILE multinaries edition – 2012" in SpringerMaterials, (accessed 15 June 2022) (2016).
[19] Cr7C3 crystal structure: Datasheet from "PAULING FILE multinaries edition – 2012" in SpringerMaterials, (accessed 15 June 2022) (2016).
[20] Mo2C (MoC0.5 ht2) crystal structure: Datasheet from "PAULING FILE multinaries edition – 2012" in SpringerMaterials, (accessed 15 June 2022) (2016).
[21] S. Gražulis, D. Chateigner, R.T. Downs, A.F.T. Yokochi, M. Quirós, L. Lutterotti, E. Manakova, J. Butkus, P. Moeck, A. Le Bail, Crystallography Open Database – an open-access collection of crystal structures, J. Appl. Crystallogr. 42 (4) (2009) 726–729, https://doi.org/10.1107/S0021889809016690.
[22] G. Greczynski, J. Lu, J. Jensen, I. Petrov, J.E. Greene, S. Bolz, W. Kölker, C. Schiffers, O. Lemmer, L. Hultman, Metal versus rare-gas ion irradiation during Ti1-xAlxN film growth by hybrid high power pulsed magnetron/dc magnetron co-sputtering using synchronized pulsed substrate bias, Journal of Vacuum Science & Technology A 30 (6) (2012) 061504, https://doi.org/10.1116/1.4750485.
[23] K. Klotz, H.-A. Bahr, H. Balke, T. Göbel, S. Menzel, U. Bahr, G. Kirchhoff, K. Wetzig, Creep analysis and laser-induced cracking of (Ti, Al)N coatings, Thin Solid Films 413 (1–2) (2002) 131–138, https://doi.org/10.1016/S0040-6090(02)00334-6.
[24] M. Sokol, J. Yang, H. Keshavan, M.W. Barsoum, Bonding and oxidation protection of Ti2AlC and Cr2AlC for a Ni-based superalloy, J. Eur. Ceram. Soc. 39 (4) (2019) 878–882, https://doi.org/10.1016/j.jeurceramsoc.2018.10.019.
[25] S. Heinze, Investigation to the oxidation behavior, interdiffusion and phase evolution of Cr2AlC thin films with IN718 substrate, oral lecture at MSE, Darmstadt (2016).
[26] S. Gaudet, C. Coia, P. Desjardins, C. Lavoie, Metastable phase formation during the reaction of Ni films with Si(001): The role of texture inheritance, J. Appl. Phys. 107 (9) (2010) 093515, https://doi.org/10.1063/1.3327451.
[27] Z. Zhang, Y. Qian, J. Xu, J. Zuo, M. Li, Effect of annealing on microstructure evolution and corrosion resistance of an amorphous Cr-Al-C coating, Corros. Sci. 178 (2021) 109062, https://doi.org/10.1016/j.corsci.2020.109062.
[28] W. Kraus, G. Nolze, POWDER CELL – A program for the representation and manipulation of crystal structures and calculation of the resulting X-ray powder patterns, J. Appl. Crystallogr. 29 (3) (1996) 301–303, https://doi.org/10.1107/S0021889895014920.
[29] J. Rodríguez-Carvajal, Recent advances in magnetic structure determination by neutron powder diffraction, Phys. B 192 (1–2) (1993) 55–69, https://doi.org/10.1016/0921-4526(93)90108-I.
[30] C. Tang, M. Steinbrück, M. Klimenkov, U. Jäntsch, H.J. Seifert, S. Ulrich, M. Stüber, Textured growth of polycrystalline MAX phase carbide coatings via

thermal annealing of M/C/Al multilayers, Journal of Vacuum Science & Technology A 38 (1) (2019) 013401, https://doi.org/10.1116/1.5131544.
[31] M.W. Barsoum, M.A.X. Phases, Properties of Machinable Ternary Carbides and Nitrides, Wiley-VCH Verlag GmbH & Co. KGaA, Weinheim, Germany, 2013.
[32] R.F. Bunshah, Handbook of Deposition Technologies for Films and Coatings Science, Technology, and Applications, Noyes Publications, Park Ridge, N.J., 1994.
[33] D.N. Lee, Textures and structures of vapor deposits, J. Mater. Sci. 34 (11) (1999) 2575–2582, https://doi.org/10.1023/A:1004696531491.
[34] H. Rueß, J. Werner, Y. Unutulmazsoy, J.W. Gerlach, X. Chen, B. Stelzer, D. Music, S. Kolozsvari, P. Polcik, T.E. Weirich, J.M. Schneider, Effect of target peak power density on the phase formation, microstructure evolution, and mechanical properties of Cr2AlC MAX-phase coatings, J. Eur. Ceram. Soc. 41 (3) (2021) 1841–1847, https://doi.org/10.1016/j.jeurceramsoc.2020.10.072.
[35] B.-Q. Fu, W. Liu, Z.-L. Li, Calculation of the surface energy of hcp-metals with the empirical electron theory, Appl. Surf. Sci. 255 (23) (2009) 9348–9357, https://doi.org/10.1016/j.apsusc.2009.07.034.
[36] U.F. Kocks, H.-R. Wenk, A.J. Beaudoin, H. Mecking, C.N. Tomé, C.N. Tomé (Eds.), Texture and Anisotropy: Preferred Orientations in Polycrystals and Their Effect on Materials Properties, first paperback edition (with corrections) Edition, Cambridge University Press, Cambridge, 2000, includes bibliographical references and index.
[37] Y. Wang, J. Huang, Texture analysis in hexagonal materials, Mater. Chem. Phys. 81 (1) (2003) 11–26, https://doi.org/10.1016/S0254-0584(03)00168-8.
[38] I. Arganda-Carreras, V. Kaynig, C. Rueden, K.W. Eliceiri, J. Schindelin, A. Cardona, H. Sebastian Seung, Trainable Weka Segmentation: A machine learning tool for microscopy pixel classification, Bioinformatics 33 (15) (2017) 2424–2426. doi:10.1093/bioinformatics/btx180.
[39] J. Schindelin, I. Arganda-Carreras, E. Frise, V. Kaynig, M. Longair, T. Pietzsch, S. Preibisch, C. Rueden, S. Saalfeld, B. Schmid, J.-Y. Tinevez, D.J. White, V. Hartenstein, K. Eliceiri, P. Tomancak, A. Cardona, Fiji: An open-source platform for biological-image analysis, Nat. Methods 9 (7) (2012) 676–682, https://doi.org/10.1038/nmeth.2019.
[40] J.C. Schuster, H. Nowotny, C. Vaccaro, The ternary systems: CrAlC, VAlC, and TiAlC and the behavior of H-phases (M2AlC), J. Solid State Chem. 32 (2) (1980) 213–219, https://doi.org/10.1016/0022-4596(80)90569-1.
[41] G. Ying, X. He, M. Li, W. Han, F. He, S. Du, Synthesis and mechanical properties of high-purity Cr2AlC ceramic, Materials Science and Engineering: A 528 (6) (2011) 2635–2640, https://doi.org/10.1016/j.msea.2010.12.039.